

# IMPACT OF CORNER GEOMETRY ON THE SECONDARY FLOW IN TURBULENT DUCTS

**Alvaro Vidal**

Department of MMAE  
Illinois Institute of Technology  
Chicago, IL 60616  
avidalto@hawk.iit.edu

**Ricardo Vinuesa**

Linné FLOW Centre  
KTH Mechanics  
Stockholm, Sweden  
rvinuesa@mech.kth.se

**Philipp Schlatter**

Linné FLOW Centre  
KTH Mechanics  
Stockholm, Sweden  
pschlatt@mech.kth.se

**Hassan M. Nagib**

Department of MMAE  
Illinois Institute of Technology  
Chicago, IL 60616  
nagib@iit.edu

## ABSTRACT

In the present study we perform direct numerical simulations (DNSs) of fully-developed turbulent square ducts with round corners at  $Re_{\tau,c} \simeq 180$  and 360, and rectangular ducts of width-to-height ratios of 3 and 5 with rounded side walls at  $Re_{\tau,c} \simeq 180$ . The friction Reynolds number  $Re_{\tau,c}$  is based on the centerplane friction velocity and the half-height of the duct. The results are compared with the corresponding duct cases with  $90^\circ$  corners. We focus on the influence of the rounding on the mean cross-stream secondary flow and on further characterizing the mechanisms that produce it. Unexpectedly, the rounded ducts exhibit higher cross-flow rates and their secondary vortices relocate near the transition point between the straight and curved walls. This behavior is associated to the statistically preferential arrangement of sweeping events entering through the curved wall, which trigger an ejection on the adjacent straight wall. We have yet to find effective modifications to the corners or transverse ends of a rectangular duct that would render better rigorous modeling of two-dimensional channel flows.

## INTRODUCTION

One of the most noticeable characteristics of turbulent flow through enclosed straight ducts with rectangular cross-section is the presence of secondary flows near the corners. These secondary flows, which are entirely due to turbulence, are known as Prandtl's secondary motions of the second kind and describe the in-plane ( $y-z$ ) mean cross-flow perpendicular to the streamwise direction  $x$ . The magnitude of the cross-flow is relatively weak compared with the streamwise velocity but strong enough to significantly affect the turbulent flow statistics (Bradshaw, 1987).

In square ducts, the cross-flow consists of two counter-rotating vortices per duct quadrant that drive the cross-flow into the corner through the bisector and out of it through the buffer-layer region in the wall-tangent direction. Therefore, the mean in-plane streamfunction  $\Psi$  is anti-symmetrically distributed with respect to the corner bisector. The underlying physical mechanisms that generate the Prandtl's secondary flow of the second kind in square ducts have been addressed by many authors. The secondary flow is associated with the secondary Reynolds shear-stress  $\overline{vw}$  and the anisotropy of the cross-stream deviatoric Reynolds-stress  $v^2 - w^2$ ; e.g., see Moinuddin *et al.* (2004). According to Perkins (1970), the deviations due to the secondary normal stress operate like a source term in the mean streamwise vorticity  $\Omega_x$  transport equation (1), and the second term in equation (2) acts as a transport term. In these equations,  $v$  and  $w$  are the wall-normal and spanwise fluctuating velocity components and their equivalents in capital letters refer to their mean quantities. The wall-tangent velocity fluctuations become more constrained as the corner is approached, increasing the source term in the equation. Near the corner, Huser & Biringen (1993) associated the Reynolds-shear stress components  $\overline{uv}$  and  $\overline{uw}$  with the transfer of momentum between the streamwise and the cross-stream normal stresses due to the inhomogeneous in-

teraction between bursting events arising from the horizontal and vertical walls. The authors also related the nonzero secondary shear stress  $\overline{vw}$  to the transport of momentum from the spanwise velocity fluctuations along the horizontal wall to the vertical fluctuations along the vertical wall and vice versa. Later, Pinelli *et al.* (2010) showed that high-speed streaks have a statistically preferential location in the near-corner region, thereby transferring momentum from the streamwise to the cross-stream fluctuations in this region. The authors also found that a low-speed streak is preferentially located at each flank of the high-speed streak on each of the perpendicular walls. They related the mean streamwise vorticity distribution to the preferred buffer-layer location of the quasi-streamwise vortices associated with the inhomogeneously distributed streaks. Therefore, this mean quantity should scale in viscous units. However, their study showed that the mean in-plane stream function scales in outer units. This behavior rather agrees with the non-local nature of the Poisson equation (3), which relates both quantities, and highlights the multiscale character of the secondary flow.

$$v \frac{\partial \Omega_x}{\partial y} + w \frac{\partial \Omega_x}{\partial z} = S(y, z) + Re^{-1} \left( \frac{\partial^2 \Omega_x}{\partial y^2} + \frac{\partial^2 \Omega_x}{\partial z^2} \right), \quad (1)$$

$$S(y, z) = \frac{\partial^2}{\partial y \partial z} (\overline{v^2} - \overline{w^2}) - \left( \frac{\partial^2}{\partial y^2} - \frac{\partial^2}{\partial z^2} \right) \overline{vw}. \quad (2)$$

$$\left( \frac{\partial^2 \Psi}{\partial y^2} + \frac{\partial^2 \Psi}{\partial z^2} \right) = -\Omega_x. \quad (3)$$

Prandtl's secondary motions of the second kind were studied by Vinuesa *et al.* (2014, 2015b) in rectangular ducts with varying aspect ratio  $AR$  (defined as the duct total width divided by its total height) using a similar numerical approach to the one presented in this study. The same authors performed direct numerical simulations (DNSs) at  $Re_{\tau,c} \simeq 180$ , which is the friction Reynolds number based on the centerplane friction velocity and the half-height of the duct, for  $AR$  between 1 and 14.4, and at  $Re_{\tau,c} \simeq 360$  for  $AR = 1$  and 3. They compared their results with the spanwise-periodic channel by Jiménez *et al.* (2004) and concluded that aspect ratios larger than 10 are required to obtain channel-like conditions in the centerplane region.

In the present study, we use a rounding radius (defined as the radius of the corner divided by the half-height of the duct) of  $r = 0.5$  to smooth the  $90^\circ$  corners of the square duct and of  $r = 1$  to substitute the straight side walls of the rectangular ducts by a half-pipe. Doing so, we expect to minimize interaction between bursting events and homogenize the distribution of the velocity streaks

along the wall. Note that in square ducts the  $r = 1$  case corresponds to the round pipe, where there are no corner effects and the flow statistics are two-dimensional due to azimuthal symmetry. DNSs of turbulent pipe flow at various Reynolds numbers were performed by El Khoury *et al.* (2013) using a similar numerical approach. We compare the cross-flow distribution in the curved ducts with the corresponding  $90^\circ$ -corner cases by Vinuesa *et al.* (2014, 2015b) and analyze its impact on the mean streamwise velocity and the wall-shear stress distribution. Finally, we study the primary and secondary shear-stress components of the rotated Reynolds-stress tensor to gain more insight into the mechanisms that produce the secondary flow.

## NUMERICAL SIMULATIONS

DNSs of the turbulent duct cases, which are summarized in Table 1, have been performed using the numerical code Nek5000, developed by Fischer *et al.* (2008) at Argonne National Laboratory. The code utilizes the spectral-element method (SEM), originally proposed by Patera (1984), to spatially discretize the incompressible Navier–Stokes equations subject to the corresponding boundary conditions. The cases under consideration have been computed using periodic boundary conditions in the homogeneous streamwise direction and no-slip boundary conditions at the walls. The SEM provides the geometrical flexibility we need to discretize the round corners using finite elements with rounded edges, while preserving the high-order accuracy of spectral methods, which is required to properly resolve the scale disparity of turbulent flows. Therefore, the mesh has been designed to satisfy the standard resolution criteria for DNS with at least three and fourteen grid-points located below  $y^+ = 1$  and 10, respectively. The superscript ‘+’ denotes inner scaling in terms of the friction velocity  $u_\tau = \sqrt{\tau_w/\rho}$  (where  $\tau_w$  is the wall-shear stress and  $\rho$  the fluid density). Similarly, the maximum and minimum spacing in viscous units between the spectral nodes of the largest elements is  $\Delta_x^+ \simeq (4, 20)$  in the streamwise direction and  $\Delta_{y,z}^+ \simeq (2, 10)$  in the vertical/spanwise directions. Note that within each element the velocity grid points follow the Gauss–Lobatto–Legendre (GLL) distribution since the basis functions correspond to Lagrange interpolants of order  $N$  for velocity and  $N - 2$  for pressure. In all of the cases presented in Table 1 we use a polynomial order of  $N = 11$ .

Table 1. Summary of the cases considered in the present study. The case notation consists of the nominal  $Re_{\tau,c}$ , the AR of the duct and the letter r if  $r \neq 0$ .

Case	AR	$Re_{\tau,c}$	$r$	$L_x/h$	$(t_a U_b L_x/h)$
180AR1	1	178	0	25	7148
180AR1r	1	183	0.5	50	595
360AR1	1	356	0	25	3652
360AR1r	1	350	0.5	25	560
180AR3	3	178	0	25	5964
180AR3r	3	191	1	25	1350
180AR5	5	177	0	25	3744
180AR5r	5	178	1	25	1400

Regarding the temporal discretization, the nonlinear terms are

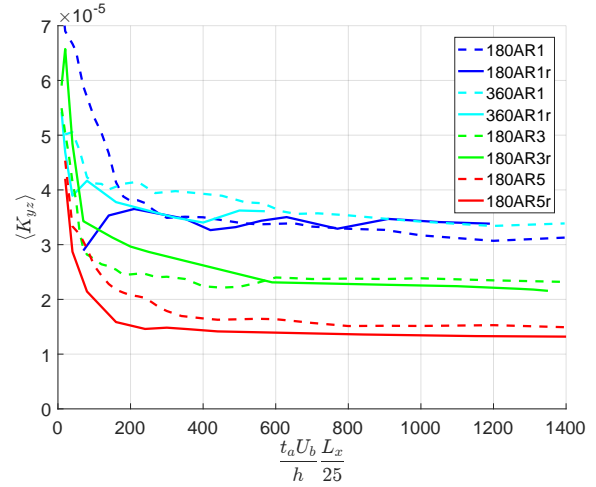


Figure 1. Cross-sectional averaged kinetic energy of the secondary flow  $\langle K_{yz} \rangle$  as a function of the averaging time  $t_a$  for the duct cases under study. Solid and dashed lines are used to indicate cases with sharp and rounded corners, respectively.

treated explicitly by third-order extrapolation (EXT3) and the viscous terms are treated implicitly by a third-order backward differentiation scheme (BDF3). High-order splitting is used to decouple pressure and velocity. One Helmholtz problem is solved for each velocity component using conjugate gradients. After that, the pressure is obtained by solving a consistent Poisson problem through generalized minimum residuals (GMRES). Nek5000 is written in Fortran77/C and employs the message-passing interface (MPI) for parallelism. The code is highly parallelizable allowing one to distribute the problem to thousands of processors in order to accommodate the high computational cost associated with large-scale direct numerical simulations.

The averaging periods used to calculate the time averaged statistics are shown in Table 1 expressed in convective time units. However, the mean flow statistics are computed by averaging not only in time but also in the homogeneous streamwise direction. Therefore, to facilitate comparison between the 180AR1r duct (with  $L_x = 50h$ ) and the rest of the ducts (with  $L_x = 25h$ ) we will consider the effective averaging time to be proportional to the streamwise length of the duct. The issues of initial transient identification and required averaging times are discussed by Vinuesa *et al.* (2016) for the  $90^\circ$ -corner duct flows. Despite the lower averaging periods of the rounded duct cases, these are long enough to obtain a nearly converged cross-sectional averaged kinetic energy of the mean cross-flow  $\langle K_{yz} \rangle = 1/A \int_a K dA$  (where  $A$  is the cross-sectional area of the duct), as shown in Figure 1. The kinetic energy of secondary flow is defined as  $K = 1/2 (V^2 + W^2)$ , where  $V$  and  $W$  are the vertical and spanwise velocity components averaged in the streamwise direction and in time for an averaging period of  $t_a$ . Finally, the converged mean flow statistics must be symmetric with respect to the various symmetry planes. Thus, the effective averaging time is further increased by exploiting the flow symmetries of the averaged velocity components, i.e., the 8 and 4 symmetries present in the square and rectangular ducts, respectively.

## CHARACTERIZATION OF THE SECONDARY CROSS-FLOW

As discussed by Vinuesa *et al.* (2015a), the strength of the cross-flow can be characterized by its mean kinetic energy  $\langle K_{yz} \rangle$ . In the rectangular cases, the asymptotic value of  $\langle K_{yz} \rangle$ , shown in Figure 1, is slightly lower in the duct with rounded side walls.

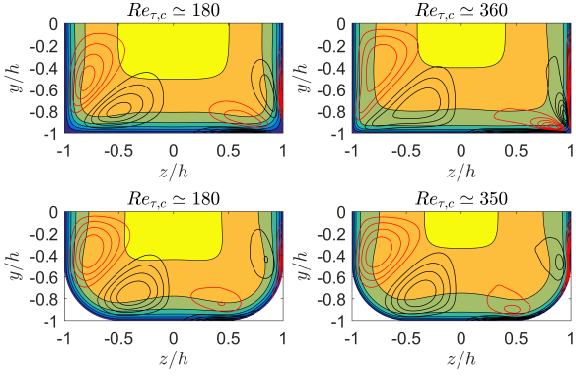


Figure 2. Color plots showing the streamwise mean velocity scaled with the bulk velocity  $U/U_b$  (7 contours with increments of 0.2). (Left half of each panel) mean streamfunction  $\Psi/(U_b h)$  (8 contours with increments of  $0.5 \times 10^{-3}$ ) and (right half of each panel) mean streamwise vorticity  $(\Omega_x h)/U_b$  (12 contours with increments of 0.1) scaled with the half-height of the duct and the bulk velocity. The red and black lines correspond to clockwise and anticlockwise sense of rotation, respectively. The value of  $Re_{\tau,c}$  from each case is indicated in the corresponding panels.

However, in the square duct cases, the rounding radius leads to a slightly higher value of  $\langle K_{yz} \rangle$  at  $Re_{\tau,c} \simeq 180$  and to a similar value at  $Re_{\tau,c} \simeq 360$ . Therefore, the results show that the impact of the corner and side wall geometry on the magnitude of the mean cross-flow is less significant than originally expected, since the secondary flow is not present in round pipes ( $r = 1$ ) and channels, where  $\langle K_{yz} \rangle = 0$ . Nevertheless, the impact of the corner geometry on the cross-flow distribution is very important, as will be discussed in the following sections.

### Square duct with round corners

The streamfunction of the mean cross-flow  $\Psi$ , shown on the left side of each panel in Figure 2 for the square duct cases, is useful to gain insight into the behavior of the secondary flow. The figure shows that the rounding radius displaces the distribution of  $\Psi$  away from the corner towards centerplane of the duct, with its peaks located near the end of the straight walls. Consequently, the separation between the streamlines of the cross-flow increases near the corner bisector ( $z = y$ ) and decreases near the centerplane indicating that the cross-flow magnitude attenuates and amplifies in these regions, respectively. The cross-flow redistribution causes the isolines of the mean streamwise velocity  $U$ , also shown in Figure 2, to become more distorted near the centerplane as more low-velocity fluid from the near-wall region is being convected by the increased wall-normal centerplane velocity into the core of the duct. This reduced mean velocity near the wall actually leads to a reduced wall-shear stress value in the centerplane. On the other hand, the isolines of  $U$  near the corner bisector become almost parallel to the curved wall.

Another interesting effect of the rounding radius is the reduced influence of the Reynolds number on the distribution of  $\Psi$  in the duct with round corners, as can be seen by comparing the left and right sides of Figure 2. This effect is also present in the maximum value of the cross-stream function  $\Psi_{max}$ , which is associated with the total cross-flow rate. This value decreases from  $2.3 \times 10^{-3}$  to  $2.0 \times 10^{-3}$  in the  $90^\circ$ -corner ducts as  $Re_{\tau,c}$  is increased from 180 to 360 but remains constant at  $\Psi_{max} \simeq 2.5 \times 10^{-3}$  in the round corner ducts. As the Reynolds number increases, the isolines of  $\Psi$  stretch farther into the  $90^\circ$  corner. Note that this corner type produces a

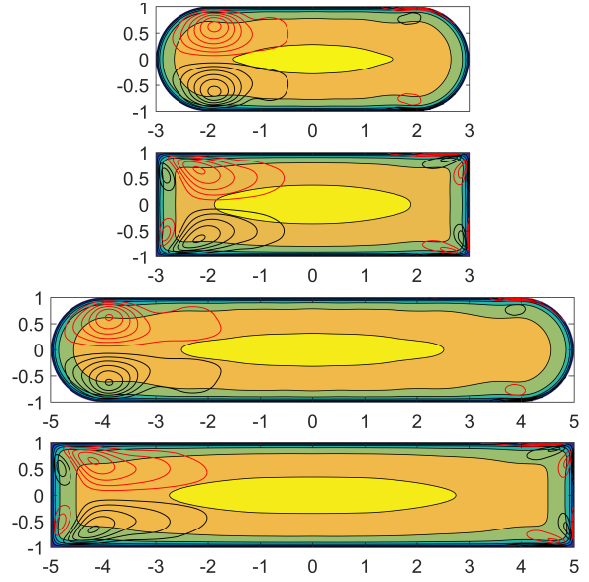


Figure 3. Color plots showing the streamwise mean velocity scaled with the bulk velocity  $U/U_b$  (7 contours with increments of 0.2). (Left half of each panel) mean streamfunction  $\Psi/(U_b h)$  (12 contours with increments of  $0.75 \times 10^{-3}$ ) and (right half of each panel) mean streamwise vorticity  $(\Omega_x h)/U_b$  (12 contours with increments of 0.1) scaled with the half-height of the duct and the bulk velocity. The red and black lines correspond to clockwise and anticlockwise sense of rotation, respectively.

region of low wall-shear stress near the corner due to the boundary layer overlapping of the adjacent walls. This region becomes smaller as the Reynolds number increases allowing for further interaction between bursting events arising from each of the walls, as discussed by Huser & Biringen (1993), thereby increasing the value of  $\Psi$  in the near-corner region. However, Pinelli *et al.* (2010) showed that the peaks of  $\Psi$  scale in outer units highlighting the role of the larger scales in the production of cross-flow and its multiscale nature. Therefore, the rounding radius may be filtering the inhomogeneous interaction of the smallest structures with spanwise length of order  $\lambda_s \ll r$ , while enhancing the inhomogeneous interaction between the largest and more energetic scales, where  $r \leq \lambda_l \leq h$ . Note that raising  $Re$  increases the separation between the different scales, such that  $\lambda_s/r \rightarrow 0$  and  $\lambda_l/r$  remains constant.

Pinelli *et al.* (2010) also showed that the streamwise vorticity distribution in  $90^\circ$ -corner ducts is determined by the preferential arrangement of the buffer-layer structures, thus, this quantity must scale in viscous units. The streamwise vorticity  $\Omega_x$ , shown on the right side of each panel in Figure 2, is characterized by the presence of four relative extrema with alternating sense of rotation and anti-symmetric distribution with respect to the corner bisector. The sense of rotation of  $\Omega_x$  changes in the buffer-layer, at  $y^+ \simeq 10$ , where the cross-flow is maximum and parallel to the wall. Therefore, the distribution of  $\Omega_x$  has an inner peak below the buffer-layer, where  $\Omega_x$  reaches its maximum value at the wall, and a counter-rotating outer peak is established above it. Our results show that this behavior is common in both the round and the  $90^\circ$ -corner ducts. However, the rounding radius has an important effect on the magnitude and distribution of  $\Omega_x$ , which becomes more apparent with increasing Reynolds numbers. In the  $90^\circ$ -corner ducts, increasing the friction Reynolds number from  $Re_{\tau,c} \simeq 180$  to  $Re_{\tau,c} \simeq 360$  causes the maximum value of the outer-scaled streamwise vorticity to rise from 0.75 at  $z \simeq 0.65h$  to 1.6 at  $z \simeq 0.83h$ . Therefore, the magnitude of

the inner peak is increased by a factor of 2.1 and its location is displaced farther into the corner. A similar behavior is observed in the outer peak. On the other hand, in the round corner ducts, the inner and outer peaks remain located in the transition region between the curved and straight walls. Moreover, the maximum value of  $\Omega_x$  is only multiplied by a factor of 1.6 (from 0.7 to 1.1). The outer peak is even more affected by the rounding radius and its magnitude remains almost constant. This behavior could indicate that some of the smallest structures may no longer be contributing to the production of cross-flow.

### Rectangular duct with round side walls

As the aspect ratio of the duct increases, the secondary vortices that are attached to the horizontal walls become stronger and reach farther in the spanwise and vertical directions. Note that  $\Psi = 0$  and  $\Omega_x = 0$  at the symmetry planes because the cross-flow must be parallel to these planes. Consequently, their counter-rotating neighbors in the adjacent vertical straight walls become weaker and increasingly attached to the wall. Interestingly, substituting the straight side walls by a semi-pipe with  $r/h = 1$  eliminates these smaller vortices, as shown in Figure 3. Therefore, the cross-flow in ducts with round side walls consists of only two counter-rotating vortices located at each side of the duct. These vortices convect the flow and associated velocities from the core of the duct towards the round side walls and from the horizontal walls towards the core. The streamlines of the cross-flow come closer to each other near the horizontal symmetry plane and the junction point between the straight and curved walls, indicating that the magnitude of the cross-flow is higher in these regions. The center of the vortices and the point of maximum cross-flow magnitude are also located near the region of transition from straight to curved walls, which highlights the important role of curvature changes on the production of these vortices. In spite of the reduction in the number of vortices, the remaining ones become stronger, increasing the total cross-flow rate from the centerplane to the sidewalls and reaching farther into the core of the duct. In the  $AR = 3$  and  $AR = 5$  cases,  $\Psi_{max}$  rises from  $3.8 \times 10^{-3}$  to  $4.7 \times 10^{-3}$  and from  $3.8 \times 10^{-3}$  to  $4.6 \times 10^{-3}$ , respectively. The enhanced cross-flow reaches farther into the center of the duct, lifting the isolines of the streamwise velocity from the wall, as can be observed in Figure 3. Therefore, the flow becomes less two-dimensional near the centerplane!

The inner and outer peaks of the streamwise vorticity are also located in the transition point between the straight and round walls. The maximum vorticity value is reduced due to the rounding from  $\Omega_x = 0.72$  to  $\Omega_x = 0.61$  and from  $\Omega_x = 0.65$  to  $\Omega_x = 0.51$  in the cases with  $AR = 3$  and 5, respectively. Also, note that the magnitude of the outer peak is halved. Again, this behavior highlights the importance of the larger structures in the production of cross-flow over the smaller scales, that are present in the near-corner region of the  $90^\circ$ -corner ducts, since the round side walls hinder inhomogeneous interaction between the latter.

### WALL-SHEAR STRESS DISTRIBUTION

The rounding radius prevents the wall-shear stress  $\tau_w$  from plunging to zero at the corner, due to the overlapping vertical and horizontal boundary layers, as shown in Figure 4. The coordinate  $s$  in this figure measures the distance from the vertical centerplane ( $x = 0$ ) along the perimeter of the duct. Note that the coordinate spans the surface between the centerplane and the closest symmetry plane, i.e., the corner bisector ( $y = \pm x$ ) if  $AR = 1$  and the horizontal centerplane ( $y = 0$ ) if  $AR > 1$ . Thus,  $s \equiv z$  in the straight surface and its maximum value corresponds to  $1/8$  and  $1/4$  of the perimeter of the square and rectangular ducts, respectively. With this definition, the sharp corner is located at  $s/h = AR$  and the transition between

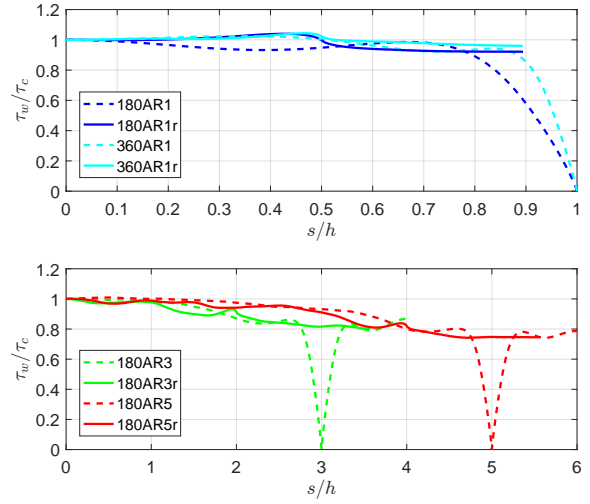


Figure 4. Wall-tangent distributions of the wall-shear stress normalized with the centerplane value  $\tau_c$ .

straight and curved surfaces at  $s/h = AR - r/h$ .

As discussed by Pinelli *et al.* (2010), the position of the local maximum and minimum values of the  $\tau_w$  distribution correspond to the statistically preferred location of high- and low-velocity streaks respectively. Note that in the pipe and channel cases, where  $\tau_w(s)$  is constant, there are no preferential locations for velocity streaks due to the azimuthal and spanwise periodicities. On the other hand, a high-speed streak is always situated near the sharp corners, where a local maximum of  $\tau_w$  occurs. As the Reynolds number increases the streak approaches the corner while maintaining a distance of around 60 viscous units. In the  $AR = 1$   $90^\circ$ -corner ducts shown in Figure 4 (top), the local maximum of  $\tau_w$  is displaced from  $s/h \simeq 0.67$  to  $0.83$  as the nominal  $Re_{\tau,c}$  is increased from 180 to 360, therefore, keeping this distance. Figure 4 (bottom) shows that a similar behavior is found in the  $AR > 1$  cases, where the two local maxima, situated at each side of  $s/h = AR$ , correspond to the same high-speed streak.

Our results in rounded ducts show that the distribution of  $\tau_w$  gradually rises near the end of the straight wall and quickly drops right before the beginning of the curved region, with an inflection point located in the transition between the two walls. In fact,  $\tau_w$  exhibits an absolute maximum value near the transition point of the  $AR = 1$  ducts, as shown in Figure 4 (top). The exact location of the maximum is less sensitive to the Reynolds number. As  $Re_{\tau,c}$  increases, its location slightly approaches the transition point, moving from  $s/h \simeq 0.43$  to  $0.46$ . Interestingly, the inner-scaled distance between the location of the peak and the transition point is  $\Delta s^+ \simeq 10.5$  in the three cases with inner-scaled radius  $r^+ \simeq 180$ . In the 180AR1r case, where  $r^+ \simeq 90$ , this distance corresponds to 12.8 viscous units.

Pinelli *et al.* (2010) also showed that the high-velocity streak is flanked by two low-speed streaks located at each of the adjacent walls. The distance between the low- and high-velocity streaks roughly corresponds to half the average inner-scaled spanwise length of the bursting cycle, i.e.,  $\Delta s^+ \simeq 50$ . Our results with round walls show that a low-velocity streak is always situated in the straight wall roughly at this distance from the high-speed streak, as indicated by the position of the local minimum of  $\tau_w$  in this region. In the round wall, however, the other low-speed streak is not always located close to the transition point.

Vinuesa *et al.* (2014) showed that in rectangular ducts a pattern of preferentially distributed high/low-velocity streaks is formed

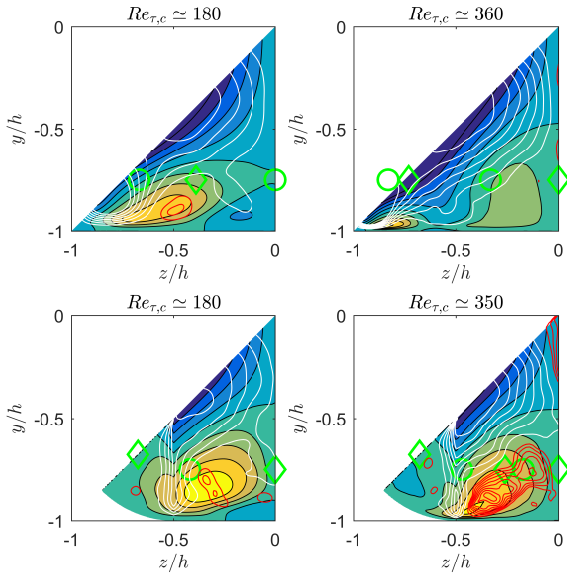


Figure 5. Secondary Reynolds-shear stresses  $\overline{u_x u_t}$  and  $\overline{u_n u_t}$  scaled with the centerplane friction velocity. Color plots showing  $\overline{u_x u_t}$  (9 contours with increments of 0.05). Red contours of  $\overline{u_n u_t} > 0$  with increments of  $3 \times 10^{-3}$  and white contours of  $\overline{u_n u_t} < 0$  with increments of 0.01. The maxima and minima of  $\tau_w$  along the wall are indicated by circles and diamonds, respectively.

starting from the high-speed streak situated near the corner. This behavior is reflected in the oscillations of the wall-shear stress distribution, which decay with the inner-scaled distance to the corner. The pattern, which is also present in our results, can be better appreciated in Figures 5 and 6, where the position of the high- and low-speed streaks along the wall is marked with circles and diamonds, respectively. The figure shows that streaks are distributed throughout the walls in pairs. Each pair consists of a high- and a low-speed streak that is oriented such that the high-speed streak is positioned closest to the side wall. Note that a special situation occurs in sharp corners, where one high-speed streak belongs to two different couples located on each of the adjacent walls. This pattern is affected by the combined effect of marginally turbulent flow effects and the presence of symmetry planes, where the wall-shear stress distribution must exhibit a local extrema. Marginally turbulent flow effects have been documented in straight ducts by Uhlmann *et al.* (2007). These effects are present if the inner-scaled width of the duct  $W_d^+$  is not long enough to fit at least 4 simultaneous streaks. Note that  $W_d^+$  grows with higher  $AR$  and/or  $Re_{\tau,c}$ , allowing more streaks to be simultaneously present in the wall. Therefore, these effects are particularly important in the 180AR1r, case where the inner-scaled curved and straight parts are too short to fit 4 streaks simultaneously.

### CROSS-FLOW GENERATION MECHANISMS

Further insight on the mechanisms that produce the cross-flow can be gained by analyzing the secondary Reynolds-shear stresses. Note that these components of the Reynolds-stress tensor are zero in pipe and channel flow due to the periodicity of the wall-tangent direction. We have rotated the Reynolds-stress tensor of the curved duct cases in the  $y-z$  plane such that  $u_n$  and  $u_t$  are the wall-normal and wall-tangent fluctuating velocities with respect to the closest wall. The wall-normal and wall-tangent directions are considered positive into the core of the flow and in the anti-clockwise direction, respectively. In  $AR > 1$  straight ducts, however, there is no simple way to rotate the tensor as the corner bisector is not a symmetry plane. Therefore, in these cases  $n$  and  $t$  refer to the vertical and

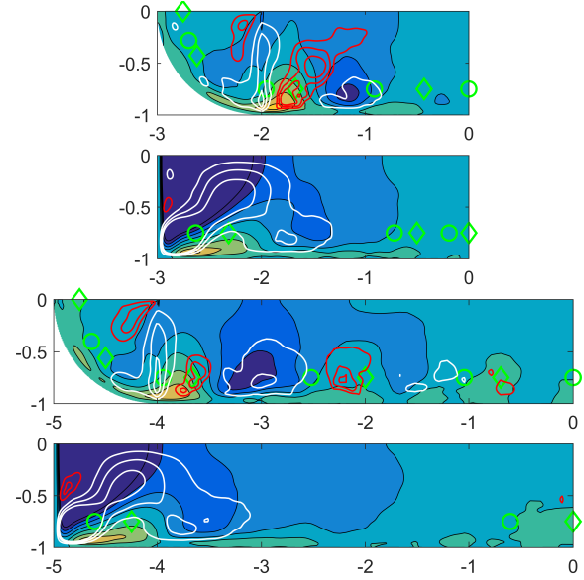


Figure 6. Secondary Reynolds-shear stresses  $\overline{u_x u_t}$  and  $\overline{u_n u_t}$  scaled with the centerplane friction velocity. Color plots showing  $\overline{u_x u_t}$  (9 contours with increments of 0.05). Red contours of  $\overline{u_n u_t} > 0$  with increments of  $3 \times 10^{-3}$  and white contours of  $\overline{u_n u_t} < 0$  with increments of 0.01. The maxima and minima of  $\tau_w$  along the horizontal and curved walls are indicated by circles and diamonds, respectively.

horizontal directions. Doing so, we can compare the distributions of  $\overline{u_x u_t}$  and  $\overline{u_n u_t}$ , in curved and straight ducts, which are shown in Figures 5 and 6.

Huser & Birnigen (1993) used quadrant analysis to study the nonzero distributions of  $\overline{u_x u_t}$  and  $\overline{u_n u_t}$ . According to them, the high value of  $\overline{u_x u_t} > 0$  and  $\overline{u_n u_t} < 0$  near the sharp corner is produced by inhomogeneous interaction between bursting events arising from the adjacent walls. However, these regions are also present in the curved ducts, despite the absence of sharp corners. Interestingly, the distributions of  $\overline{u_x u_t}$  and  $\overline{u_n u_t}$  exhibit a similar pattern to the one found in streak pairs and discussed in the previous section. The  $\overline{u_x u_t} > 0$  region is located below each pair and flanked by a region of  $\overline{u_x u_t} < 0$ . Similarly, the positive and negative regions of  $\overline{u_n u_t}$  are located close to the high- and low-speed members of each pair. The correlations are stronger near the sharp corner and the transition between straight and curved walls, and decay towards the vertical centerplane of the ducts.

This behavior can be explained by considering the instantaneous vortices associated to the streaks. In curved ducts, as the energetic structures in the core of the duct ( $u_x > 0$ ) approach the curved walls ( $u_n < 0$ ), they must turn in the wall-tangent direction ( $u_t > 0$ ) generating  $\overline{u_x u_t} > 0$  and  $\overline{u_n u_t} < 0$ , and then leave the wall ( $u_n > 0$ ) producing  $\overline{u_n u_t} > 0$ . Therefore, the regions of  $\overline{u_x u_t} > 0$  are associated to the preferential position of high-speed sweeps. These sweeps drag low-momentum fluid ( $u_x < 0$ ) from the near-wall region triggering an ejection that is responsible for the adjacent  $\overline{u_x u_t} < 0$  region at a rough distance of 100 viscous units. Notice that this ejection causes the cross-stream lines to lift away from the wall in this region, as shown in Figure 3. Also, the ejection tilts towards the side walls ( $\overline{u_n u_t} < 0$ ), distorting the isolines of  $U$  slightly farther in this direction. This ejection is in turn responsible of promoting the appearance of an adjacent sweep located farther towards the vertical centerplane. This behavior leads to a decaying pattern of preferentially-arranged alternating sweeps and ejections,

which is responsible for cross-flow production along the wall. The corresponding pattern of instantaneous vortices is shown by Vinuesa *et al.* (2015b) in rectangular straight ducts using short averaging periods. Notice that the negative regions of  $\overline{u_n u_t} < 0$  are much stronger than the positive ones and extend farther away from the wall, since they are caused by the large energetic structures from the core of the duct, which can only approach the side walls in the negative wall-tangent and wall-normal directions. The  $\overline{u_n u_t} > 0$  and  $\overline{u_x u_t} > 0$  regions, however, are generated by the sweep within the near-wall region. Therefore, they are scaled in viscous units, as shown in Figure 5.

The sharp corners lead to a more complex interaction between the turbulent structures and the wall. Sweeps entering the sharp corners through the corner bisector must also tilt in the wall-tangent direction, i.e., either the vertical or the horizontal directions. The region of  $\overline{u_x u_t} > 0$  on the bottom wall is produced when they tilt in the horizontal direction. However, this region is smaller and weaker than in the corresponding curved cases. This weakening and wall-confinement is even more apparent at higher Reynolds numbers, as shown in Figure 5. One explanation for this is that the sweep will also trigger an ejection ( $u_x < 0$ ) on the vertical wall, which tilts towards the horizontal wall ( $u_t > 0$  and  $u_n < 0$ ) generating  $\overline{u_n u_t} < 0$  near the corner, and  $\overline{u_x u_t} < 0$  above the horizontal wall, as shown by Huser & Biringen (1993). The ejections that tilt from the left wall towards the bottom wall ( $u_n < 0$ ) counteract the effect of the sweeps that turn in the vertical direction ( $u_n > 0$ ) and oppose the mean cross-flow momentum in the region. Therefore, this type of interaction could be responsible for the lower mean cross-flow rates found in ducts with sharp corners.

## CONCLUSIONS

Direct numerical simulations (DNSs) of fully-developed turbulent rounded ducts are carried out using the spectral element code Nek5000 to study the impact of the rounding on the secondary flow and better characterize the mechanisms that produce it. We have considered square ducts with round corners, at  $Re_{\tau,c} \simeq 180$  and 360, and rectangular ducts of width-to-height ratios 3 and 5 with round side walls, at  $Re_{\tau,c} \simeq 180$ . The results are compared with the corresponding 90°-duct cases showing that the rounding radius increases the total cross-flow rate from the core of the duct towards the walls. These results were initially unexpected since the mean cross-flow is not present in round pipes. The extrema of the in-plane stream function  $\Psi$  and the streamwise vorticity  $\Omega_x$  relocate near the transition point between the two walls with different curvature. Also, the distributions of  $\Psi$  and  $\Omega_x$  become less sensitive to changes in the Reynolds number, which highlights the role of the larger structures in generating the secondary flow.

Considering the rounded ducts, the relative extrema of the wall-shear stress show that preferentially arranged high- and low-speed streak pairs are distributed throughout the wall, starting from a high-speed streak situated in the curvature transition point. A similar pattern is observed in the distribution of the positive and negative secondary Reynolds-shear stresses. Both patterns can be associated to the preferential location of a sweeping event close to the curvature transition point. In the cases with  $AR > 1$ , the sweep triggers an ejection in the adjacent straight wall, which tilts towards the side walls. The ejection is responsible for the distortion of the isolines of  $\Psi$  and  $U$  at  $\Delta z \simeq 1$  from the curvature transition point. This pattern, which repeats in a decaying manner towards the vertical centerplane, eventually generates the mean cross-flow. Additional interaction between bursting events is present in the near-corner region of the 90°-corner ducts leading to a secondary cross-flow distribution that is more sensitive to the Reynolds number. Some of these interactions counteract the effect of the sweeps and oppose

the local mean cross-flow, which explains the lower cross-flow rates found in these cases.

So far our computations with parametric configurations of various rectangular ducts with increasing aspect ratios, starting from the square duct case, and with various rounding of corners and end walls, have yet to reveal clues on how best to design a channel flow in the laboratory.

## ACKNOWLEDGEMENTS

Computer time was provided by Argonne Leadership Computing Facility at Argonne National Laboratory, which is supported by the Office of Science of the US Department of Energy. AV and HN acknowledge the support of the John T. Rettaliata Chair at IIT. RV and PS acknowledge the financial support from the Swedish Research Council (VR) and the Knut and Alice Wallenberg Foundation.

## REFERENCES

- Bradshaw, P. 1987 Turbulent secondary flows. In *Annual Review of Fluid Mechanics*, , vol. 19, pp. 53–74.
- El Khoury, G. K., Schlatter, P., Noorani, A., Fischer, P. F., Brethouwer, G. & Johansson, A. V. 2013 Direct numerical simulation of turbulent pipe flow at moderately high Reynolds numbers. *Flow, Turbulence and Combustion* **91**, 475–495.
- Fischer, P. F., Lottes, J. & Kerkemeier, S. 2008 Nek5000 Web page <http://nek5000.mcs.anl.gov> .
- Huser, A. & Biringen, S. 1993 Direct numerical simulation of turbulent flow in a square duct. *Journal of Fluid Mechanics* **257**, 65–95.
- Jiménez, J., del Álamo, J. C. & Flores, O. 2004 The large-scale dynamics of near-wall turbulence. *Journal of Fluid Mechanics* **505**, 179–199.
- Moinuddin, K. A. M., Joubert, P. N. & Chong, M. S. 2004 Experimental investigation of turbulence-driven secondary motion over a streamwise external corner. *Journal of Fluid Mechanics* **511**, 1–23.
- Patera, A. T. 1984 A spectral element method for fluid dynamics: laminar flow in a channel expansion. *Journal of Computational Physics* **54**, 468–488.
- Perkins, H. J. 1970 The formation of streamwise vorticity in turbulent flow. *Journal of Fluid Mechanics* **44**, 721–740.
- Pinelli, A., Uhlmann, M., Sekimoto, A. & Kawahara, G.L 2010 Reynolds number dependence of mean flow structure in square duct turbulence. *Journal of Fluid Mechanics* **664**, 107–122.
- Uhlmann, M., Pinelli, A., Kawahara, G. & Sekimoto, A. 2007 Marginally turbulent flow in a square duct. *Journal of Fluid Mechanics* **588**, 153–162.
- Vinuesa, R., Noorani, A., Lozano-Durán, A., El Khoury, G. K., Schlatter, P., Fischer, P. F. & Nagib, H. M. 2014 Aspect ratio effects in turbulent duct flows studied through direct numerical simulation. *Journal of Turbulence* **15**, 677–706.
- Vinuesa, R., Prus, C., Schlatter, P. & Nagib, H. M. 2016 Convergence of numerical simulations of turbulent wall-bounded flows and mean cross-flow structure of rectangular ducts. *Meccanica* **51**, 3025–3042.
- Vinuesa, R., Schlatter, P. & Nagib, H. M. 2015a Characterization of the secondary flow in turbulent rectangular ducts with varying aspect ratio. In *Proceedings of the 9th International Symposium on Turbulence and Shear Flow Phenomena, TSFP-9*, pp. 1–6. Melbourne, Australia.
- Vinuesa, R., Schlatter, P. & Nagib, H. M. 2015b On minimum aspect ratio for duct flow facilities and the role of side walls in generating secondary flows. *Journal of Turbulence* **16**, 588–606.